Formation and persistence of ponderomotive plasma gratings created by finite-duration laser pulses

Götz Lehmann, Sophie Opara, and Karl H. Spatschek
Institut für Theoretische Physik I, Heinrich-Heine-Universität Düsseldorf, D 40225 Düsseldorf, Germany

(Received 16 June 2026; accepted 22 October 2026; published 6 November 2026)

Prompted by early experimental realizations of plasma-optical components, we examine how finite formation times affect the quality and scaling behavior of a plasma grating induced by the ponderomotive potential of two counter-propagating pump laser beams. Ponderomotively driven gratings provide an alternative to ionization gratings, which offer significant advantages in terms of stability and contrast, but exhibit notable drawbacks regarding repetition rates and material modification. Here, in addition to parameters discussed in prior work, we identify the pump pulse duration τ_p as another factor for the dynamics and persistence of ponderomotively driven plasma gratings. Based on full Vlasov simulations we predict the maximum density grating amplitude as well as its lifetime as a function of electron temperature T_e and laser pulse duration τ_p. For interpretation and modeling, we use a generalized form of a known one-frequency kinetic model to a finite-bandwidth scenario. Based on these investigations we predict the influence of τ_p and T_e on the maximum achievable grating performance, providing a detailed explanation of the observed grating scaling. As a general result, we find that even gratings generated by laser pulses of less than a few hundred femtoseconds duration τ_p allow for very efficient utilization up to picoseconds, provided that the plasma temperature is not too high (e.g., $T_e \leqslant 100\,\mathrm{eV}$).

DOI: 10.1103/9237-5stj

I. INTRODUCTION

More than 180 years ago, Lord Kelvin (William Thomson) was already discussing how electrically neutral particles can be moved by electric fields. The history of the ponderomotive force is told, for example, in the book by Heinrich Hora [1], with the emphasis, of course, on the fact that it is a nonlinear force. This is where the laser [2] and modern laser physics come into play. Through discoveries honored with Nobel Prizes in physics [3,4], it became possible to generate very short pulses with extremely high fields. Laser-plasma physics thus became one of the most innovative areas of modern physics. Indestructible plasma optics [5], manipulation of light by light [6], and plasma photonics [7], to name just a few, became the buzzwords used to characterize the ensuing research aimed at exploiting ultra-high-power coherent light sources.

Changes in the plasma density under the action of strong laser fields were investigated at an early stage, e.g., in Refs. [8–10]. Subsequently, numerous studies have outlined potential routes toward highly specific practical applications. These range from photonic crystals in general to laser compressors in particular, although theoretical investigations still considerably outnumber experimental demonstrations. The Refs. [11–38] cited here are by no means exhaustive and, inevitably, reflect a subjective snapshot of the field. It is clear hope that in the future plasma optical components can be employed at high intensities, being as effective as classical ones which can be used only at lower intensities [39].

Experimental verification of plasma Bragg gratings has been clearly demonstrated in experiments, particularly in gases. Plasma gratings are formed when two or more coherent, high-intensity laser beams interfere in a gaseous medium, producing a spatially periodic intensity pattern. When the laser intensity exceeds the ionization threshold, this pattern is transferred into a periodic modulation of free-electron density, creating a plasma grating. The grating period is determined by the laser wavelength and the crossing angle of the beams. It should be emphasized that ionization gratings differ from gratings being produced by the ponderomotive force in already ionized media. Thus, in principle ionization plasma gratings and ponderomotive plasma gratings originate from distinct physical mechanisms of laser-medium interaction. Ionization plasma gratings are formed through spatially modulated ionization of a neutral medium, leading to plasma density maxima that coincide with the maxima of the laser intensity interference pattern. These gratings can persist beyond the laser pulse duration. In contrast, ponderomotive plasma gratings arise from the redistribution of preexisting free electrons driven by the ponderomotive force, resulting in plasma density minima at the laser intensity maxima and density maxima at the intensity minima. As a consequence, ponderomotive plasma gratings are out of phase with the driving intensity pattern. This opposite phase relationship is a crucial experimental signature. The most direct experimental evidence of plasma gratings is obtained using a pump-probe configuration. Intersecting pump beams generate the plasma grating, while a time delayed, weak probe

Published by the American Physical Society under the terms of the Creative Commons Attribution 4.0 International license. Further distribution of this work must maintain attribution to the author(s) and the published article's title, journal citation, and DOI.

beam is diffracted by the periodic plasma structure. Observation of diffraction orders at angles consistent with Bragg diffraction provides clear confirmation of the grating's existence. Importantly, probe diffraction persists after the pump pulses have ended, distinguishing plasma gratings from instantaneous Kerr (optical) gratings. Additional verification is achieved through interferometric and phase-contrast imaging, which reveal periodic phase shifts associated with the negative refractive index change induced by free electrons. Time-resolved measurements of diffraction efficiency allow determination of the plasma grating lifetime, typically ranging from several picoseconds to nanoseconds, governed by electron recombination and diffusion. Polarization-independent behavior further confirms the plasma origin of the grating. Looking back over recent years [40–44], it is fair to conclude that the experimental development of plasma-optical components has advanced substantially, and that a transition to widespread adoption now appears realistically within reach.

Here we will concentrate on detailed numerical analysis and theoretical interpretation of ponderomotively driven plasma gratings (being produced by finite duration pumps), with the aim of establishing criteria for their effective applicability as a function of the governing parameters. An important issue, for instance, concerns the question of whether ponderomotively driven plasma gratings exist only during the laser plasma interaction time and how the phase relationship develops during existence time. We will show here that even for small pump duration (parameter τ_p) the ponderomotively driven initial phase of a grating will change into a pressure balanced grating which shows similarity with an ionization grating.

In a series of papers [22,23,26,45,46], Peng *et al.* investigated various aspects of ponderomotively driven plasma gratings. This work led to a fairly comprehensive understanding of lattice formation as a function of key physical parameters. A major breakthrough was the classification of the different lattice structures in terms of two parameters ν and μ. The parameter ν is defined as

$$\nu \equiv \frac{\omega_{\mathrm{pe0}}^2}{2k_1^2 v_0^2}, \quad v_0 = a_0 c, \quad a_0 = \frac{eA_0}{m_e c}, \tag{1}$$

where ω_{pe0} is the electron plasma density evaluated at the average electron particle density n_{e0}, and A_0 is the maximum of the laser vector potential. The grating wave number is $2k_1$ (k_1 is the wave number in plasma of the oppositeley propagating driving laser pulses). In our subsequent evaluations, we assume $\nu > 1$. The trapping (superradiant) case $\nu < 1$ was discussed in Ref. [21]. Variations in laser amplitudes can be expressed in ν.

The other fundamental parameter is

$$\mu \equiv \frac{3T_e}{m_e v_0^2}. \tag{2}$$

It depends on the electron temperature T_e. Using macroscopic (hydrodynamic) models and PIC simulations, supplemented by kinetic calculations including finite ion temperature effects, promising experimental parameter windows were identified by Peng *et al.* [22,23] by varying μ in the regime $\nu > 1$. In the present paper, we consider both $\mu > 1$ as well as $\mu \to 0$. When pointing at the electron temperature (T_e) scaling, we might use μ variation for fixed v_0.

As already suggested, during grating formation another parameter is significant:

$$\tau_p \equiv \text{pulse duration of pump pulses.} \tag{3}$$

For definition see Appendix A. For simplicity, we assume two counter-propagating pump pulses of same duration τ_p in an already existing plasma of electron density n_{e0} and electron temperature T_e. An alternative configuration is also feasible, namely, a combination of long and short pump pulses. The methods proposed here will apply also to that case

The starting point and primary focus of this work is a series of Vlasov simulations carried out as a function of the parameters ν, μ, and τ_p. Expressed in physical variables, our investigation concentrates mainly on the dependence of the system behavior on pulse duration (τ_p) and electron temperature (T_e). We distinguish between short- and long-pulse regimes, separated by the ion response time. Characteristic trends are identified in both the grating amplitude and the grating lifetime, together with distinct scaling behavior as a function of electron temperature. A second focus of the work is the interpretation and modeling of these findings. We build on a model originally proposed by Michel *et al.* [47–49] for the low-bandwidth regime, and extend it to a finite frequency interval. Given the linearity of the model and the neglect of dissipative effects, we obtain remarkably good agreement with the observed behavior.

Accordingly, the paper is structured as follows. Section II presents the Vlasov simulation results. Section III develops the theoretical interpretation and finite-bandwidth model. Finally, Sec. IV summarizes the main findings.

II. VLASOV SIMULATION RESULTS

A. Typical temporal grating evolution as a function of the parameter τ_p

In this section we present Vlasov-Maxwell simulations for the temporal evolution of ponderomotively driven gratings. To this end, we use our semi-implicit Maxwell-Vlasov code [50]. The pump pulse duration τ_p is varied. First, we will discuss the case of a grating driven by ("infinitely") long laser pulses with pulse duration $\tau_p \gg T_{pi}$, where $T_{pi} \equiv 2\pi/\omega_{pi}$ is the typical timescale for ion motion being determined by the ion plasma frequency ω_{pi}. We then consider pump pulses with duration shorter than T_{pi}. In all cases, we choose the laser wavelength to be $\lambda_0 = 800\,\mathrm{nm}$ and use linear polarization.

Apart from the laser pulse duration, all simulation parameters are identical in the following two subsections. We consider an initially homogeneous underdense plasma slab of plasma density $n_0 = 0.05\,n_c$, bounded by regions of vacuum. Here n_c is the critical density following from $\omega_0 \equiv \omega_{\mathrm{pe0}}$. The slab has a length of $30\,\lambda_0$, it is centered around $x = 20\,\lambda_0$. We assume fully ionized hydrogen plasma, i.e., $m_i = 1836\,m_e$, $Z = 1$, and initial charge neutrality, i.e., electron and ion density, are the same ($n_i = n_e$). The laser propagates along x, which is resolved with 50 grid points per λ_0. The initial plasma temperature is set to $T_e = 50\,\mathrm{eV}$ for electrons and $T_i = 5\,\mathrm{eV}$ for ions. The simulation resolution in v space is such that we use $\Delta v = 0.02 v_{\mathrm{th}}$, where v_{th} is the thermal veloc-

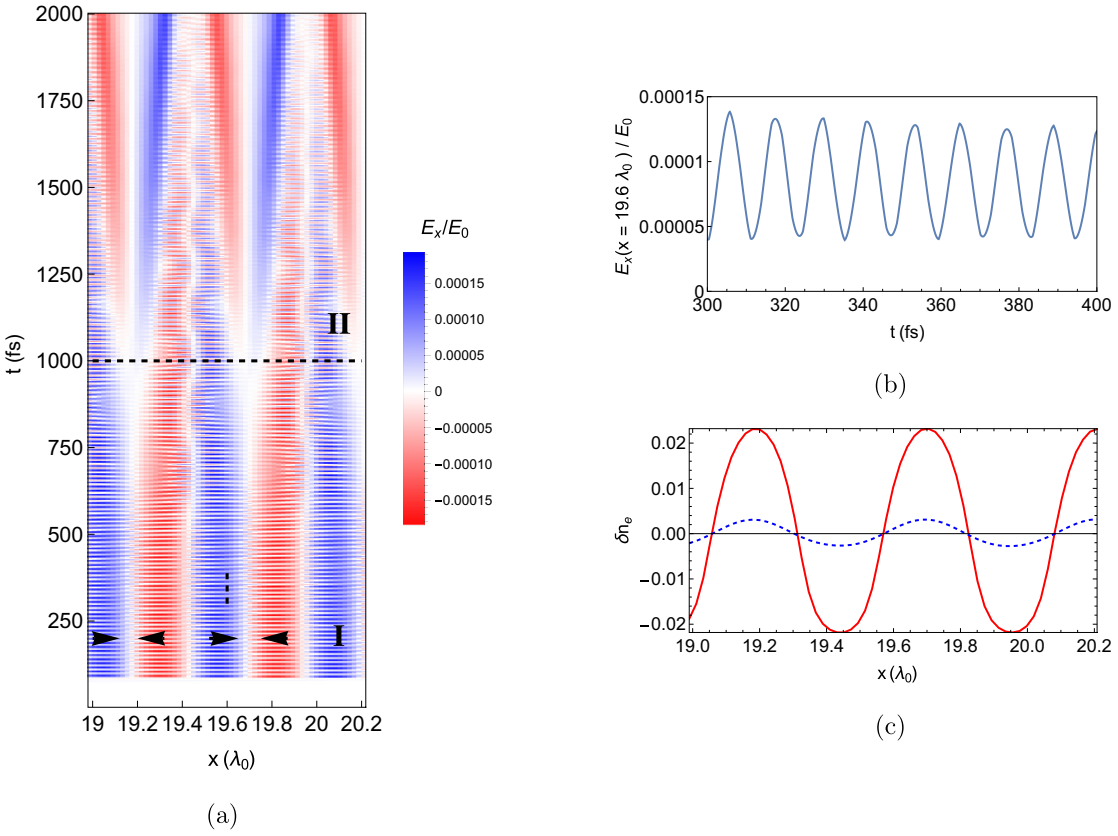


FIG. 1. Simulation results for a grating driven by very long ("infinite") laser pulses. (a) Temporal evolution of the longitudinal electric field E_x at the grating center. Shown are two spatial periods of the grating. The field dynamics is categorized in two phases I and II; see text. Arrows indicate the direction of $F = q_i E_x$. (b) Electric field at position $x = 19.6\,\lambda_0$ [indicated by vertical line in (a)] during phase I. The field oscillates with the electron plasma frequency. (c) Normalized electron density modulation δn_e at times $t = 520\,\mathrm{fs}$ (dashed blue line) and $t = 1900\,\mathrm{fs}$ (solid red line). The latter time corresponds to the maximum density variation.

ity for each species. The dimensionless laser pulse amplitude $a_0 = A_0 e/m_e c$ is $a_0 = 0.01$ (corresponding to an intensity of approx. $2 \times 10^{14}\,\mathrm{W/cm^2}$). Electric fields obtained from simulations are normalized by $E_0 = m_e c\omega_0/e \approx 4 \times 10^{12}\,\mathrm{V/m}$, and, unless otherwise stated, we use n_0 for density normalization.

For the above parameters, the relevant timescale for electrons is $T_{\mathrm{pe}} = 2\pi/\omega_{\mathrm{pe}} \approx 12\,\mathrm{fs}$, whereas $T_{pi} \approx 520\,\mathrm{fs}$. Whenever finite pulse duration is specified, it is measured as the FWHM duration of the electric field.

Summarizing in terms of the parameters ν, μ, and τ_p we assume

$$\nu = 263, \quad \mu = 0.3\text{–}35, \quad \tau_p = 100\text{–}2000\,\mathrm{fs}. \tag{4}$$

1. *Phenomenology of a "long grating" from a Vlasov simulation for $\tau_p \gg T_{pi}$*

In order to model very long laser pulses, we choose the laser field envelope to be tanh-shaped with a rise time of two field cycles. At $t = 80\,\mathrm{fs}$ the two pulses begin to overlap at the center of the plasma slab. Once the two pulses interfere, they drive a ponderomotive grating with a period $\Lambda = \frac{1}{2}\lambda_0/\sqrt{1 - n_0/n_c} \equiv \frac{1}{2}\lambda$. Note that for $n_0 = 0.05\,n_c$ we have $\lambda \approx \lambda_0$. The ponderomotive force then pushes electrons into the potential troughs, leading to the formation of a space-charge field E_x, which then acts on the ions. The ions become accelerated and begin streaming to the nodes of the standing electric wave, i.e., the ponderomotive potential troughs. This eventually leads to a plasma density modulation with period Λ, which for the above parameters reaches its maximum at $t \approx 1900\,\mathrm{fs}$.

Figure 1 summarizes results from this simulation. The temporal evolution of the longitudinal electric field E_x in a region close to the center of the plasma grating, resulting from the local imbalance of electron and ion density, is shown in Fig. 1(a). At early times $t < T_{pi}$ (phase I), the field is dominated by the electron response to the ponderomotive potential. We observe electrons oscillating about the ponderomotive potential troughs at the electron plasma frequency. Figure 1(b) shows the amplitude of E_x along the vertical dashed line of Fig. 1(a); oscillations with a period of $T_{\mathrm{pe}} \approx 12$ fs are apparent.

For times $t \gtrsim T_{pi}$ the electric field structure is first influenced and then ultimately dominated by ion motion (phase II). The influx of ions towards the electrons trapped in the laser field is triggered early; the direction of the force $F = q_i E_x$ is indicated by the arrows in Fig. 1(a). At $t \approx 1000\,\mathrm{fs}$ the electrostatic field E_x is no longer dominated by the electrons under the influence of the ponderomotive potential, but by the heavier ions now attenuating the electric field (e.g., $x \approx 19.2\,\lambda_0$) and eventually overshooting these positions. During the later stage of phase II, we observe that the local electric

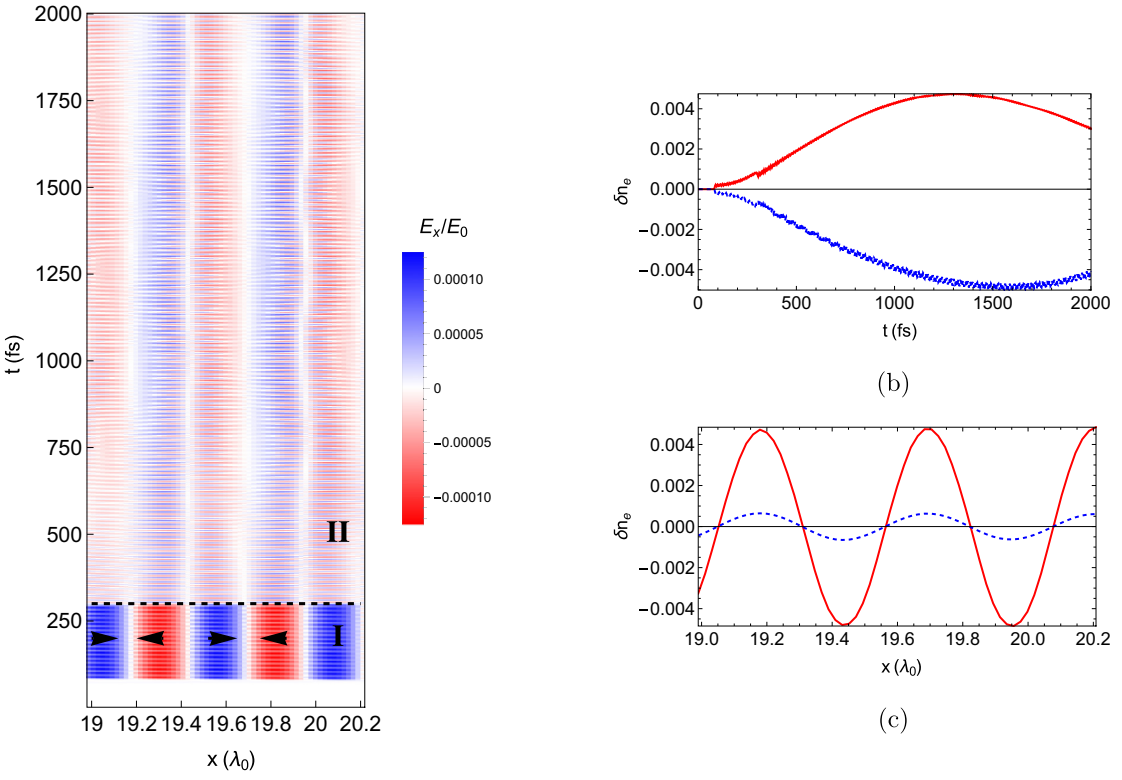


FIG. 2. Temporal evolution of the electric field E_x for the case of finite-duration pump pulse of duration $\tau_p = 250\,\text{fs} < T_{pi}$. The maximum density variation is reached at $t \approx 1300$ fs. Simulation parameters are otherwise the same as for the results shown in Fig. 1(a). Temporal evolution of the longitudinal electric field E_x at the grating center. Phase I is limited by the laser pulse duration. Field reversal occurs immediately after the laser pulse overlap ends. (b) Maximum (red) and minimum (blue) of δn_e in the grating center as a function of time. (c) δn_e in the center of the grating at $t = 250$ fs (blue dashed line) and $t = 1300$ fs (red solid line).

field reverses and that the field maximum moves outwards with a characteristic velocity [visible as tilted blue and red stripes in Fig. 1(a)].

Figure 1(c) shows the electron density modulation $\delta n_e = n_e - n_0$ at two times. The dashed blue line shows the modulation at $t \approx 520$ fs. The solid red line shows the maximum density modulation at $t \approx 1900$ fs.

2. *Phenomenology of a "short grating" from a Vlasov simulation for $\tau_p \leqslant T_{pi}$*

Figure 2 shows a typical result for an (initially ponderomotively driven) short grating generated by short pump pulses. The only change with respect to the previous subsection is that the laser pulses are now super-Gaussian in time with a FWHM duration of $\tau_p \approx 250$ fs. A super-Gaussian envelope is used rather than a Gaussian envelope to define the pulse duration more sharply. The main interaction between the pulses takes place between $t \approx 100$ fs and $t \approx 300$ fs, yet, the density maximum appears at approximately $t \approx 1300$ fs. Notably, the electric field (as indicated by the color scale) changes its sign after the ponderomotive potential has vanished, while the grating is still (and remains) clearly structured. This phase shift is clearly related to the absence of the ponderomotive force during the later development.

For such short driving times, phase I is purely electron dominated. Even though the force acting on the electrons reverses direction during phase II, the density modulation continues to grow because of ion inertia; see Figs. 2(b) and 2(c).

B. Scaling results from Vlasov simulation

1. *Time for reaching maximum amplitude and performance at maximum density*

In the Vlasov simulations, we measured the time $t_{\max}$ that elapses until the maximum of the grating density is reached. We discuss how this time varies with pulse duration τ_p and electron temperature T_e (always keeping the initial ion temperature $T_i = T_e/10$). In Fig. 3 $t_{\max}$ is shown as a function of T_e for different values of τ_p. For Fig. 1, $t_{\max}$ is 1900 fs, whereas the simulation corresponding to Fig. 2 yields a value of 1300 fs. Note that in the latter case the time $t_{\max}$ is much larger than τ_p. We do not have pure electron gratings; ions take part in the dynamics. Renormalizing the values by subtracting the initial phase I, one obtains in both cases a value of approximately 900 fs up to the attainment of the density maximum during phase II.

The times $t_{\max}$ scale approximately with $1/\sqrt{T_e}$. This suggests identifying the propagation velocity of the stripes in phase II with the ion acoustic velocity c_s.

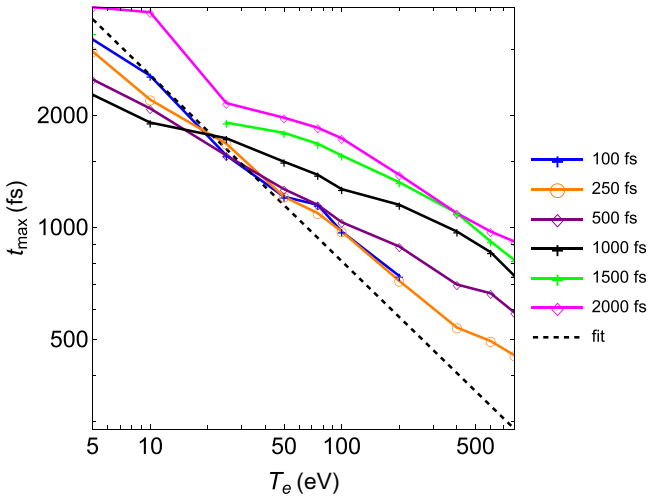


FIG. 3. Time t_{max} to reach the maximum amplitude δn as a function of electron temperature T_e for different pulse duration τ_p. The broken line is the approximation $t_{max} = \exp[9 - 0.5\log(T_e)]$.

At this point, however, we should clarify which temperature values we use in the analysis. In general, and unless stated otherwise, we use the initial electron and ion temperatures. Strictly speaking, this is not entirely correct, since the temperatures change over the course of the temporal evolution. However, the fact that our approach is not fundamentally inappropriate when determining scaling trends rather than exact values is demonstrated, for the parameter ranges considered here, by comparing the later electron and ion distribution functions with the corresponding initial distributions. Figure 4 shows a typical example, from which we can see that although the temperatures do change, the changes are not large enough to significantly alter the scaling trends. The data shown in this figure are taken from the simulation shown in Fig. 2 and shows the electron and ion distribution function, respectively, as a function of the flow-corrected velocity $\tilde{v}$ at different positions x and times t. The velocities are normalized to the thermal velocties $v_{th,e,i} = \sqrt{T_{e,i}/(m_{e,i})}$. Specifically, the distributions are shown at $t = 0$, at $t = 400$ fs (i.e., after the driver pulses just left the plasma) and at $t = 1300$ fs (the time at which the maximum grating amplitude is achieved). For the two latter times, we show data at $x_{max} = 19.2\lambda_0$ (the position at which a density maximum is located) and $x_{min} = 19.45\lambda_0$ (the location of the associated density minimum). It is apparent that the temperature changes, but not significantly for any of the distributions. The general trend is that the temperature slightly increases at density maxima and slight decreased at density minima.

As noted already by several authors (see, e.g., Ref. [23]), it would be incorrect to claim that the ponderomotively driven lattices exist only as long as the ponderomotive potential is present. The reason for this behavior lies in the ions, which move towards the electrons as long as the latter are confined. Due to their large mass the ion inertia leads to a long-lasting persistence.

Ion motion is such that, after a finite time, they either overshoot the positions at which the electrons have formerly been trapped ($\mu \ll 1$) or become deflected from these positions ($\mu \gtrsim 2$) [23]. Either way, the grating contrast (i.e., the difference in maximum and minimum of δn_e over a period) first becomes maximum and then decreases; see Fig. 2(b). However, as ions perform the same type of motion in every grating period, the overshot or reflected ions, respectively, of adjacent periods will bunch again and thus lead to a repetitive reformation of the grating.

For the application of a plasma grating, its persistence is of crucial importance. As a measure, we use the time interval $\Delta\tau^p_{max}$ during which the density modulation amplitude $\max(\delta n_e) - \min(\delta n_e)$ does not change significantly (e.g., by less than 10%) within the first temporal cycle of the grating. In Fig. 5(a) we show the typical temporal evolution of a grating modulation for a short and a long grating, respectively. For the two examples, $\Delta\tau^p_{max}$ is of the order of 700 to 1200 fs. Figure 5(b) shows the long-term temporal evolution of the grating modulation over multiple reformation cycles of the grating driven by the 250 fs laser pulses. On this timescale, the periodic nature of the grating becomes apparent. Subsequent iterations of the grating are less and less pronounced in amplitude, damping is clearly observed. The time it takes for the reoccurrence of the grating scales as $T_e^{-1/2}$, hinting at a relation to the ion sound speed.

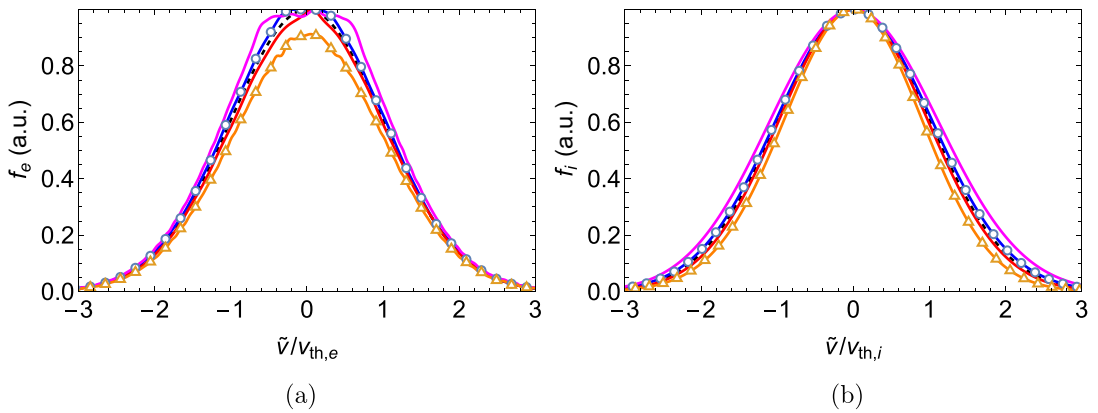


FIG. 4. Distribution functions of (a) electrons and (b) ions as a function of the flow corrected velocity $\tilde{v}$. The black dashed line shows the initial distribution at $t = 0$. The distributions at $t = 400$ fs are shown as red solid (for $x = x_{min}$) and blue solid line with circles (for $x = x_{max}$). Distributions at $t = 1300$ fs are shown as orange (light gray) line with triangles (for $x = x_{min}$) and magenta (medium gray) solid line at $x = x_{max}$.

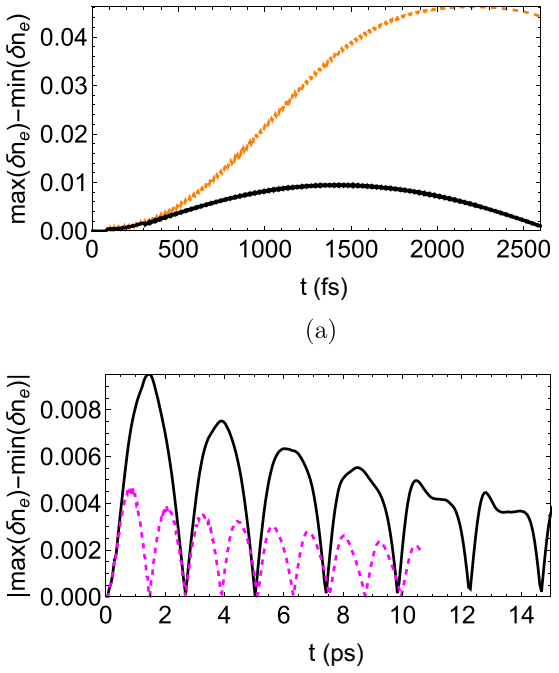


FIG. 5. (a) Temporal evolution of plasma density modulation amplitude $|\max(\delta n_e) - \min(\delta n_e)|$ for long (orange dashed) and short (black solid) gratings shown in Figs. 1 and 2, respectively. (b) Long-time evolution of $|\max(\delta n_e) - \min(\delta n_e)|$ for two short gratings in plasmas of different temperatures. The black solid line is the same case as the black line in (a) ($T_e = 50\,\text{eV}$). The magenta dashed line is for a simulation identical to that of the black line, but with $T_e = 200\,\text{eV}$.

2. *Scaling of maximum grating amplitude with electron temperature T_e and pulse duration τ_p*

We now examine in more detail the maximum grating amplitude obtained from the Vlasov simulations. We address the scaling differences between short and long gratings with respect to the parameter τ_p, in addition to the parameters μ and ν discussed earlier [22,23]. We also focus on temperature scaling.

Figure 6 shows the scaling of the maximum grating amplitude as functions of T_e and τ_p, as obtained from Vlasov simulations. For pulse duration $\tau_p \lesssim O(1000)\,\text{fs}$, the maximum grating amplitude increases with τ_p at fixed T_e. For pulse duration $\tau_p \gtrsim O(1000)$ fs, the amplitudes approach saturation, i.e., they do not increase further for fixed T_e when increasing τ_p. The dependence of the amplitude at fixed τ_p upon variation of T_e is more complex. For all pulse duration a higher temperature is accompanied by a decrease in the maximum amplitude. However, the dependence of $\max(\delta n_e)$ on T_e is different for "short" and "long" pulses. For "small" $\tau_p \leqslant 250$ fs, we find that $\max(\delta n_e) \sim T_e^m$. The exponent m can be obtained by a linear fit to the corresponding line in Fig. 6. For $\tau_p \leqslant 250\,\text{fs}$, we obtain $m \approx -0.5$, throughout the whole tested temperature range. This is consistent with earlier observations [51]. For "larger" $\tau_p \geqslant 500$ fs we observe again a power-law dependence of $\max(\delta n_e)$ with T_e, however, now the exponent is different in different temperature regimes. At

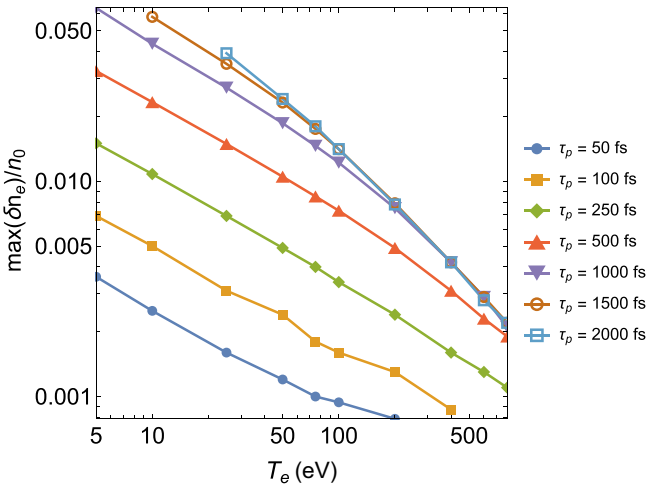


FIG. 6. Results from Vlasov simulations for the scaling of the maximum density amplitude with respect to electron temperature T_e and τ_p.

lower temperatures, $|m|$ is always smaller than towards larger temperatures. The crossover temperature where the transition from one scaling exponent to another takes place depends on the pulse duration τ_p. Let us exemplify this for the data of $\tau_p = 1000\,\text{fs}$ pulses. At temperatures $T_e \lesssim 100\,\text{eV}$ we have $m \approx -0.5$, for $T_e \gtrsim 200\,\text{eV}$ we find $m \approx -0.9$. With increasing pulse length, the crossover temperature (from $m \approx -0.5$ to $m \approx -1$ scaling) decreases.

In Fig. 7 we show in more detail the variation of the maximum density as a function of τ_p for two values of T_e. The tendency to saturate in the limit of large duration τ_p is clearly visible.The relative magnitudes are smaller for larger temperatures. Nevertheless, this evaluation shows that even with short pump duration one might obtain sufficient grating amplitudes provided the plasma temperature T_e is not too high. The observed scaling behavior will be later explained by a finite-bandwidth model.

III. INTERPRETATION AND MODELING

A. Theoretical classification of temporal dynamics

We first give a *qualitative* classification of the temporal evolution depending on pulse duration τ_p and electron

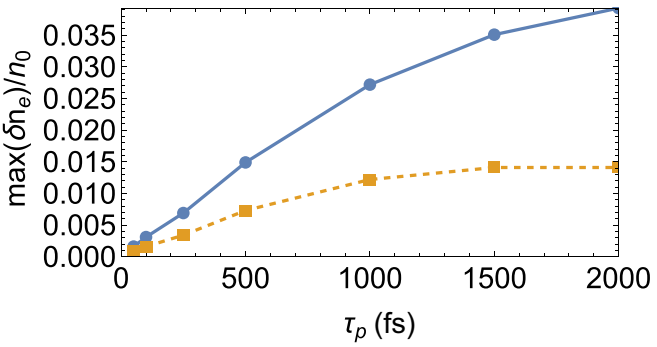


FIG. 7. Maximum density amplitude $\max(\delta n_e)$ vs. τ_p for $T_e = 25\,\text{eV}$ (blue solid line) and $T_e = 100\,\text{eV}$ (orange dashed line).

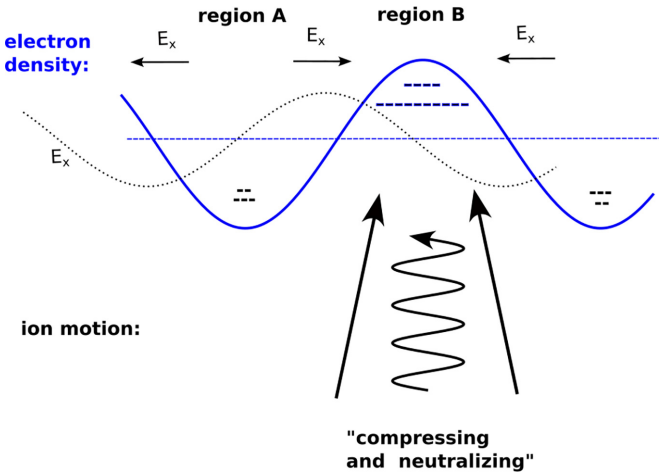


FIG. 8. Sketch of the electron density distribution $\delta n_e \sim -\varphi_p$ and the direction of the created electrostatic field E_x in case of a ponderomotively driven grating evolution. The initial reaction of the ions is also shown.

temperature T_e, i.e., we interpret the phenomena shown in Figs. 1 and 2, respectively. At this stage, we refrain from a quantitative analysis and instead focus on the key qualitative differences between the phenomena of short and long gratings.

1. Balance in the presence of a ponderomotive potential

An electron grating is established at very early times due to the action of the ponderomotive potential φ_p (early during phase I in Figs. 1 and 2). In Fig. 8 we sketch the situation in which the electrons have been pushed by the ponderomotive force and ions have just begun to move under the action of the created electrostatic fields. The ions are not yet actively involved for times $t \ll T_{pi}$ (early part of phase I). Then the electron density variation follows from

$$\delta n_e \approx \frac{\epsilon_0}{e}\frac{\partial^2 \phi}{\partial x^2}, \tag{5}$$

where ϕ is the electrostatic potential. In general, we estimate the electric field strength $E_x = -\frac{\partial \phi}{\partial x}$ from the total force on electrons

$$F_x = \underbrace{e\frac{\partial \phi}{\partial x}}_{-eE_x} - \underbrace{\frac{1}{n_e}\frac{\partial P}{\partial x}}_{F_P} - \underbrace{\frac{\partial \varphi_p}{\partial x}}_{F_p} \approx 0, \tag{6}$$

when we neglect the electron inertia [22]. We have contributions F_P from the pressure force, and $F_p = -\vec{\nabla}_x \varphi_p$ from the ponderomotive force, in addition to the electric force due to the space-charge field E_x.

Two counter-propagating linearly polarized laser beams of equal frequency and amplitude,

$$\mathbf{E}_1 = E_0 \cos(\omega t - k_1 x), \quad \mathbf{E}_2 = E_0 \cos(\omega t + k_1 x), \tag{7}$$

interfere to form a standing wave $\mathbf{E}(x,t) = 2E_0 \cos(k_1 x)\cos(\omega t)$. The cycle-averaged squared electric field is given by $\langle E^2(x,t)\rangle_t = 2E_0^2 \cos^2(k_1 x)$, resulting in an intensity distribution $I(x) = I_0 \cos^2(k_1 x)$, with $I_0 = 2c\varepsilon_0 E_0^2$. The resulting light pressure can be expressed in terms of a ponderomotive potential φ_p, which reads

$$\varphi_p(x) = \frac{e^2\langle E^2\rangle}{4m_e\omega^2} = \varphi_{p0}\cos^2(k_1 x), \quad \varphi_{p0} = \frac{e^2 E_0^2}{2m_e\omega^2}. \tag{8}$$

The ponderomotive force [52] is usually denoted as

$$\vec{F}_p = -\frac{m_e c^2}{2}\vec{\nabla}|\vec{a}|^2 \equiv -\vec{\nabla}\varphi_p, \quad \varphi_p = \frac{m_e c^2}{2}a_0^2 \cos(2k_1 x), \tag{9}$$

which agrees with the above formulation since $a \hat{=} \frac{eA}{m_e c^2} \hat{=} \frac{eE}{m_e c\omega}$. The periodic ponderomotive potential has a spatial period of $\lambda/2$ and expels electrons from the intensity maxima, leading to the formation of a ponderomotively driven plasma grating.

When we ignore the pressure P, we find

$$\delta n_e \approx \frac{\epsilon_0}{e^2}\frac{\partial^2 \varphi_p}{\partial x^2} = -2k^2\frac{\epsilon_0 m_e c^2}{e^2}a_0^2 \cos(2k_1 x) \tag{10}$$

as well as

$$E_x \approx k\frac{m_e c^2}{e}a_0^2 \sin(2k_1 x). \tag{11}$$

This distribution is shown in Fig. 8. The interpretation is consistent with the phenomena shown in Figs. 1 and 2 during phase I. Inserting numbers, we find

$$E_x \approx 4 \times 10^{10}\, a_0^2 \frac{\mathrm{V}}{\mathrm{cm}} \approx 0.0001\, E_0, \tag{12}$$

which is in excellent agreement with the Vlasov results over the duration for which the ponderomotive potential exists.

2. Transition to kinetic pressure dominance

Pressure P may dominate after the (more or less abrupt) disappearance of the pump laser pulses in ponderomotively driven short plasma gratings, or in ionization gratings once the ionization process in the gas has ended. We have an intrinsic buildup of pressure gradients during the growth of local density maxima and minima in long ponderomotively driven gratings.

In addition to the intrinsic buildup of pressure gradients during growth of local density maxima and minima (during the final formation of the grating), local heating may further reinforce the dominance of pressure. A scenario with dominant pressure force is shown in Fig. 9.

In purely pressure-dominated gratings we approximate Eq. (6) by

$$E_x \approx -\frac{1}{en_e}\frac{\partial P}{\partial x}. \tag{13}$$

The pressure can be treated either in the adiabatic or in the isothermal approximation,

$$P \sim P_e \sim n_e^\gamma. \quad \text{or} \quad P = n(T_e + T_i) \approx n_e T_e. \tag{14}$$

Since the adiabatic approximation is well justified [45], we will employ it for some later estimates. Generally, when comparing ponderomotive potential contributions with pressure contributions in (6), pressure becomes significant for $\mu \geqslant 1$; see Appendix B

When comparing Fig. 9 with Fig. 8, we recognize that relative to the density extrema the direction of the electric field

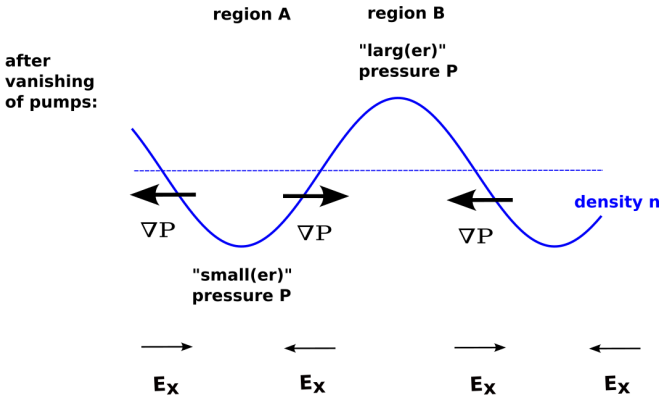


FIG. 9. Sketch of the initial electron density distribution $\delta n_e \sim -\varphi_p$ and the direction of the created electrostatic field E_x in case of kinetic pressure dominance after disappearance (or relative weakness) of a ponderomotive potential.

reverses. Both Figs. 8 and 9 will now be used to discuss the behaviors shown in Figs. 1 and 2, respectively.

3. *Initial phase I of ponderomotively driven plasma gratings*

In general, for phase I of both, long and short gratings as shown in Figs. 1 and 2, the ponderomotive lattice scenario depicted in Fig. 8 applies. Initially, the electrons are driven into the wells of the ponderomotive potential, where they accumulate, while relative minima in the electron density form at the maxima of the ponderomotive potential.

Then, during the initial phase I, the ions start moving in the direction of the electric field E_x, as indicated in Fig. 8. Neutralization of the electron density humps begins. In other words, during phase I, the electrons are confined by the ponderomotive potential and "pull" the ions. When the ions start moving, after some time (because of their large mass) they begin to dominate the dynamics, showing a pronounced inertial effect. Later, they pull the much lighter and more mobile electrons along with them.

As long as the electric field remains of the order $E_x \approx -O(\frac{\partial \varphi_p}{\partial x})$, ions are continuously accelerated. In linear approximation the ion velocity u_i, e.g., close to an electron maximum, becomes

$$m_i \frac{\partial u_i}{\partial t} \approx eE_x \quad \rightsquigarrow \quad u_i \approx \frac{e}{m_i} E_x t. \tag{15}$$

Then the ion density variation δn_i follows from

$$\frac{\partial n_i}{\partial t} + u_i \frac{\partial n_i}{\partial x} \approx -n_i \frac{\partial u_i}{\partial x} \quad \rightsquigarrow \quad \frac{1}{n_0}\frac{\partial \delta n_i}{\partial t} \approx -\frac{e}{m_i} t \frac{\partial E_x}{\partial x}. \tag{16}$$

Thus, during phase I, the density initially increases quadratically in time

$$\frac{1}{n_0}\frac{\partial \delta n_i}{\partial t} \sim 2k_1 \frac{e}{m_i} t|E_x| \quad \rightsquigarrow \quad \frac{\delta n_i}{n_0} \approx k_1 \frac{e}{m_i}|E_x| t^2. \tag{17}$$

This behavior is observed in Vlasov simulations. The motion is not straight, but oscillatory (on the ion timescale), as seen in the simulations and suggested by the field structure as sketched in Fig. 8.

The manifestation of phase I differs significantly between long and short gratings. For long gratings, as in Fig. 1, the ponderomotive potential dominates over the entire time required for the trailing ions to establish a quasineutral region in the vicinity of the density maxima. This region is clearly visible in Fig. 1 at $t \approx 1000$ fs.

For short gratings, by contrast, the ponderomotive potential is switched off after a time $t \approx \tau_p$. Beyond this point, the electrons are no longer focused by the ponderomotive force but instead follow the ions as the latter have gradually begun to move. Only up to times $t \approx \tau_p$ does the evolution in Figs. 2 and 1 coincide. Consequently, the density amplitudes in Fig. 1 at $t \approx 1000$ fs are expected to be significantly larger than those in Fig. 2 at $t \approx \tau_p$. The just mentioned density amplitudes are the initial conditions for the next phase.

4. *Ion-inertia-dominated evolution in phase II*

The ions start overshooting in phase II. This results in an electric-field reversal. The density variation reaches its maximum in phase II, when ion trajectories from neighboring regions cross. In principle, for both long and short gratings, similar but not identical forces determine the ion motion.

In long gratings, density inhomogeneities relax through collective ion dynamics. The presence of a ponderomotive force (as it occurs for long gratings) modifies this process by introducing an additional pressure-like contribution, leading to a renormalized effective sound speed. The argument proceeds as follows. Approximating the electron momentum equation by

$$\vec{E} + \frac{1}{en_e}\vec{\nabla} P_e + \frac{1}{e}\vec{\nabla}\varphi_p \approx 0, \tag{18}$$

where φ_p is the ponderomotive potential for electrons, we insert $\vec{E}$ into the ion equation of motion

$$m_i n_i \frac{\partial \vec{u}_i}{\partial t} \approx en_i \vec{E} - \vec{\nabla} P_i, \tag{19}$$

to obtain after linearization

$$\frac{\partial^2 \delta n}{\partial t^2} \approx \left[c_s^{\text{eff}}\right]^2 \nabla^2 \delta n, \tag{20}$$

with

$$c_s^{\text{eff}} \approx \sqrt{\gamma \frac{T_e}{m_i} + \frac{n_0}{m_i}\frac{\partial \varphi_p}{\partial n}} \quad \text{for} \quad T_i \ll T_e. \tag{21}$$

This approximation applies to long gratings, whereas for short gratings

$$c_s^{\text{eff}} \approx c_s = \sqrt{\gamma \frac{T_e}{m_i}} = 12.64 \times 10^5 \sqrt{T_e\,[\text{eV}]} \times 10^{-8} \frac{\text{nm}}{\text{fs}} \quad \text{for protons} \tag{22}$$

holds. For long gratings $\frac{\partial \varphi_p}{\partial n} < 0$, and the restoring velocity is weakened.

Characteristic lifetimes are shown in Fig. 3. Theoretically, we estimate lifetimes by

$$t_{\max} \approx \frac{\lambda_0/8}{c_s^{\text{eff}}}. \tag{23}$$

Within a simple estimate for $T_e \approx 50\,\mathrm{eV}$ we get $c_s \approx 9 \times 10^{-2}$ nm/fs, leading to $t_{\max} \approx O(10^3)$ fs. This estimate is close to the observed timescale. Motivated by this agreement we added (for $\varphi_p = 0$) the curve

$$\ln(t_{\max}\,[\mathrm{fs}]) \approx 9 - \tfrac{1}{2}\ln(T_e\,[\mathrm{eV}]) \tag{24}$$

to Fig. 3. The curve also reflects the statement by Peng *et al.* [23], according to which the periodicity time should be roughly inversely proportional to μ, i.e., $\sim 1/T_e$. Our observations, however, rather suggest a proportionality closer to $\sim 1/\sqrt{T_e}$. Two reasons could be responsible for a slight deviation from this proportionality which we supported by the above argument based on ion sound speed. First, there is the modified form of the effective sound speed c_s^{eff} being modified by ponderomotive effects. Second, a change in the electron temperature T_e relative to its initial value during the nonlinear evolution of the grating does occur, as illustrated by a typical example in Fig. 4. However, the change remains within a range for which the use of the initial temperature can still be considered a reasonable approximation.

Summarizing phase II for short pulses, after the pump pulses vanish for $t \geqslant \tau_p$, the scenario sketched in Fig. 9 emerges. The electric fields are then governed by the pressure gradient. The electric field distribution becomes opposite to that in the initial phase $t < \tau_p$. The electric-field strengths are considerably smaller than in the case of long pump pulses (Fig. 1). It is important to note that so-called short gratings produced by short pulses of duration τ_p persist much longer than τ_p and reach their maxima at much later times than τ_p. The reason is that in the investigated parameter regime, electron gratings evolve into quasineutral ion gratings.

B. Scaling forecast with a linear kinetic approach

We now interpret the observed Vlasov scaling in the light of a simple model. We employ a linear kinetic model that is largely based on a previous proposal by Michel *et al.* [47]. A generalization, which we refer to as the finite-bandwidth model, will provide estimates regarding the scaling of the grating amplitude with electron temperature T_e and pulse duration τ_p. However, it relies on a linearization and therefore does not capture heating effects or nonlinear saturation.

1. Kinetic one-frequency model

Michel *et al.* [47] presented a kinetic model for the electron density perturbations under ponderomotive action. The result, obtained from a linearized calculation, is

$$\frac{\delta n_{ek}(\omega)}{n_{e0}} = \frac{\epsilon_0 k^2}{e^2 n_{e0}} \underbrace{\frac{1+\chi_{ik}(\omega)}{1+\chi_{ek}(\omega)+\chi_{ik}(\omega)}\chi_{ek}(\omega)}_{F_\chi(\omega)}\,\hat{\varphi}_p, \tag{25}$$

where $\hat{\varphi}$ denotes the Fourier transform of the ponderomotive potential

$$\varphi_p = \frac{m_e c^2}{2} a_0^2\, \mathcal{E}_{a_0 a_0} \cos(2k_1 x), \quad k = 2k_1. \tag{26}$$

An evaluation of the ponderomotive potential, generated by pump pulses of finite duration, was given, e.g., in Ref. [32],

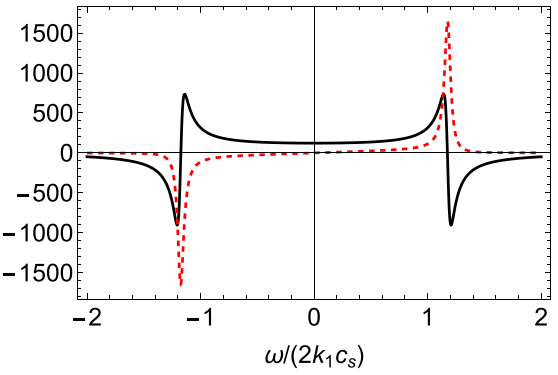


FIG. 10. Real (black solid) and imaginary parts (red dashed) of F_χ as functions of ω for $T_e = 50\,\mathrm{eV}$, $T_i = 5\,\mathrm{eV}$, and $k = 2k_1$.

together with the definition

$$\mathcal{E}_{a_0 a_0}(x,t) = e^{-\frac{x^2}{\langle x^2\rangle}}\, e^{-\frac{v_{g0}^2 t^2}{\langle x^2\rangle}} \equiv f(x,t), \tag{27}$$

which also follows from the Gaussian-pulse discussion in Appendix A. Here $\langle x^2\rangle$ is the square of the spatial width, and $\sigma_t^2 \equiv \langle x^2\rangle / v_{g0}^2$ the square of the temporal width.

It is interesting to examine the complex function F_χ as a function of ω for fixed $k \approx 2k_1$. An example is shown in Fig. 10.

Note that

$$\mathrm{Re}F_\chi(\omega = 0) = \frac{1}{k^2\lambda_{De}^2} \sim \frac{1}{T_e}, \quad \mathrm{Im}F_\chi(\omega = 0) = 0. \tag{28}$$

2. A finite-bandwidth generalization

A finite (in time) laser pulse has a finite (temporal) width τ_p, as discussed in Appendix A. The same applies to the ponderomotive potential. The ponderomotive potential φ_p of two counter-propagating Gaussian laser pump pulses is proportional to [32]

$$\varphi_p \sim \mathcal{E}_{a_0 a_0}(x,t)\cos(2k_1 x). \tag{29}$$

We compute the space-time Fourier transform of (27) in the form

$$\tilde{f}(k,\omega) = \iint_{-\infty}^{\infty} f(x,t)\, e^{-i(kx-\omega t)}\, dx\, dt$$

and leave the 2π factors for the back-transform. After separation, we find for the time integral

$$\tilde{f}(k,\omega) \sim \int_{-\infty}^{\infty} \exp\left(-\frac{t^2}{\sigma_t^2}\right) e^{i\omega t} dt$$
$$= \sigma_t \sqrt{\pi}\, e^{-\omega^2\sigma_t^2/4} \sim e^{-\omega^2/2\sigma_\omega^2}$$

with

$$\sigma_\omega^2 = \frac{2}{\sigma_t^2} = \frac{2.355^2 \times 2}{\tau_p^2} \rightsquigarrow \sigma_\omega = \frac{3.33}{\tau_p}. \tag{30}$$

If we consider frequencies in the range

$$-\Omega \leqslant \omega \leqslant \Omega, \tag{31}$$

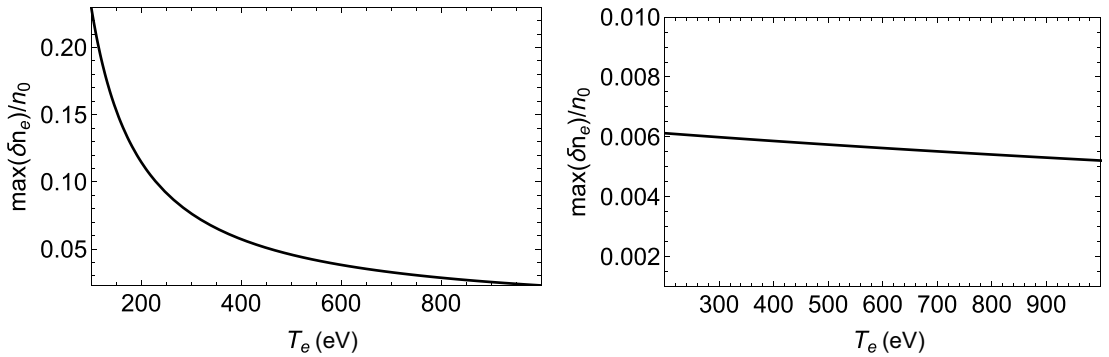


FIG. 11. Scaling predictions of a finite-bandwidth model. Shown are maximum values of $\delta n/n_0$ as functions of electron temperature T_e. (a) Result for a long pump pulse, $\tau_p = 17$ ps. The $1/T_e$ dependence is expected for $\omega = 0$. (b) Same as in (a), but now for a much shorter pulse length ($\tau_p = 170$ fs). Note the different scaling on the vertical axis.

we use

$$\Omega := \frac{\mathrm{FWHM}}{2} = \frac{2.355}{2}\sigma_\omega = \frac{3.92}{\tau_p}. \tag{32}$$

Comparing with a rectangular box distribution of length $2\,\tau_p$ in t-space, we would get the dominant spectral contribution in the region $|\omega| \leqslant \frac{\pi}{\tau_p}$, which approximately agrees with the above Gaussian estimate.

For "infinitely" long pumps of equal frequency, we would have contributions only from $\omega = 0$. Then $\delta n_e(t) \sim \delta n_e(\omega)$. However, for short pump pulses (with broader frequency range) we should integrate over the given frequency region.

We generalize the kinetic calculation [47] by averaging over a frequency domain, obtaining an effective F function. The mathematically exact procedure is to perform the inverse transform, starting from (25):

$$\frac{\delta n_e(x,t)}{n_{e0}} \sim \frac{\epsilon_0}{e^2 n_{e0}} \iint k^2 F_\chi\, \hat{\varphi}_p\, e^{i(kx-\omega t)}\, d\omega\, dk. \tag{33}$$

In the frequency integral, the factors F_χ and $\hat{\varphi}_p$ contribute. The factor $\hat{\varphi}_p$ approximately limits the integration range to $-\Omega$ to $+\Omega$. Since all numerical simulation results exhibit a clearly recognizable $\cos(2kx)$ spatial distribution, we focus here on the temporal dependence. We should now also bear in mind that the original expression was derived by linearization, and that its validity at large times is therefore questionable. At short times, the ω dependence of F is therefore expected to be of greatest importance. This, of course, constitutes an approximation that leads us to intrduce the effective F function

$$F_{\mathrm{eff}} = F_{\mathrm{eff}}(T_e, T_i, \tau_p) \equiv \frac{1}{2\Omega}\int_{-\Omega}^{+\Omega} F_\chi(\omega) e^{-\omega^2/2\sigma_\omega^2}\, d\,\omega. \tag{34}$$

Compared to the original F_χ, this accounts for the finite time duration of the pump lasers. A similar effect, caused by the finite spatial extent, will cause a broadening of the wave number $2k$. That broadening, however, will be ignored here.

Under these conditions we end up with the prediction of the electron density variations in the grating

$$\frac{\delta n_e(x)}{n_{e0}} \approx \frac{\epsilon_0 k^2}{e n_{e0}} F_{\mathrm{eff}}\, \hat{\varphi}_p \approx 2F_{\mathrm{eff}} a_0^2 \frac{n_c}{n_0} \cos(2k_1 x). \tag{35}$$

We call it a finite-bandwidth generalization of the original model of Michel *et al.* [47].

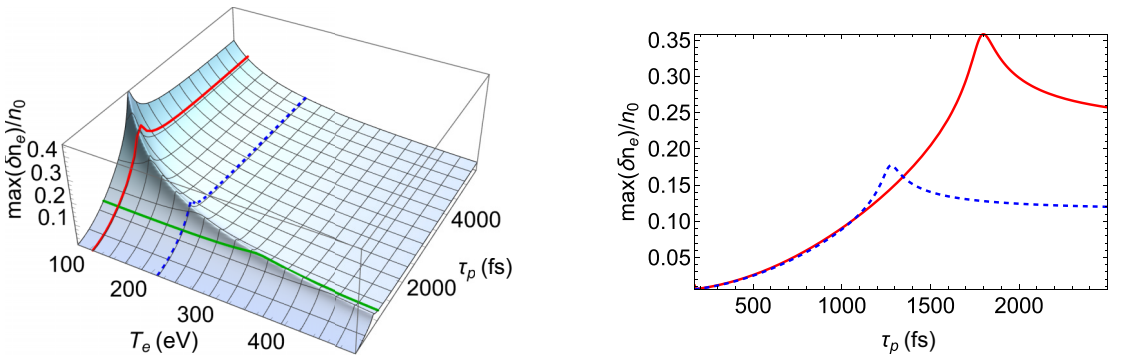
We are aware of the numerous assumptions involved in this approximate approach. For example, the time range over which the linear relationship between δn_e and the ponderomotive potential φ_p remains valid is uncertain. Moreover, the approximation adopted here does not account for phase differences between the density perturbation and the dynamics of the ponderomotive pressure. All damping effects, which, however, we do not observe on short timescales, are likewise neglected. We therefore regard the finite-bandwidth generalization primarily as a prediction of trends rather than as a quantitatively reliable long-term model.

We evaluate the finite-bandwidth model in two ways. First, we investigate the temperature dependence of the maximum achievable density variation. Figure 11 shows typical results for long and short pumps, respectively. For long pump pulses [see Fig. 11(a)], the temperature dependence is $\sim T_e^{-1}$, as has been predicted already by Michel *et al.* [47]. On the other hand, as seen from Fig. 11(b), shorter pump duration leads to two significant modifications. First, the amplitudes are substantially lower, and second, the temperature dependence is significantly weaker.

The finite-bandwidth model further yields a prediction for the dependence of the grating amplitude on pump duration. The relative increase of maximum amplitude is illustrated in Fig. 12. For a fixed temperature (e.g., $T_e = 100$ eV) and fixed pump amplitude a_0, the density maxima increase with τ_p.

We observe a fast increase of the grating amplitude with increasing (still relatively small) pump width up to a certain maximum. For longer pumps ($\tau_p \geqslant 2000$ fs), the grating amplitudes approach a (relatively large) saturation amplitude.

Summarizing so far, the qualitative trends observed in Vlasov simulations are well captured by a finite-bandwidth model. Of particular interest is the prediction of the T_e dependence of the amplitudes. For long pulses, we have $\delta n \sim T_e^{-1}$. Short pulses produce gratings of much lower amplitude with a weak temperature dependence. As a function of τ_p, the maximum achievable density amplitude initially increases strongly, but transitions into saturation at relatively large τ_p values. At least for long pulses, the kinetic model predicts the amplitude



(a) (b)

FIG. 12. (a) Prediction of the finite-bandwidth model for maximum values of $\delta n/n_0$ for a fixed electron temperature as a function of pump duration τ_p. (b) Lineouts for $T_e = \text{const}$ of the surface shown in (a) for $T_e = 100\,\text{eV}$ (red solid) and $T_e = 200\,\text{eV}$ (blue dashed), respectively. The lineout for $\tau_p = \text{const} = 1000$ fs (green solid) is shown in Fig. 13.

scaling $\delta n \sim a_0^2$. For shorter pulses a reduction of amplitudes with decreasing τ_p occurs.

However, in any case the kinetic model used here is only approximately valid—in contrast to the full Vlasov simulations. We should not expect that the model is fully quantitatively reliable during the saturation process.

3. *Crossover prediction of the finite-bandwidth model*

For very long pump pulses, the $\frac{1}{T_e}$ dependence is very nicely reproduced. For shorter pump pulses, the T_e dependence is much weaker than for long pump pulses. An algebraic dependence of the fitting curve may not be the best choice. In addition (as expected), short pulses generally result in significantly smaller amplitudes.

However, the crossover in T_e dependence from long to short pump pulses is not as smooth as the two shown examples might suggest (see Fig. 13). The model indicates the following. As long as the frequency domain lies within the kc_s borders of the F_χ function, we get a smooth variation of functional dependence $\sim T_e^{-\alpha}$ with well-defined power α. See Fig. 10 for the resonance at $\omega = kc_s$. On the other hand, when the frequency range extends significantly beyond kc_s, the T_e dependence of the maximum amplitude δn becomes very weak.

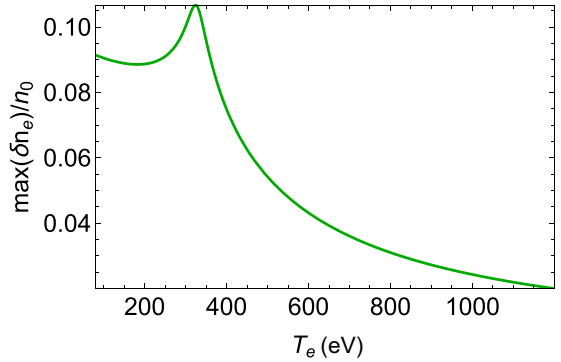


FIG. 13. Maximum δn as function of electron temperature T_e for an intermediate pump pulse length $\tau_p = 1000$ fs. The depicted T_e values include $T_e^{\text{crossover}} = 400\,\text{eV}$.

This domain can be estimated with the help of (32),

$$\frac{3.92}{\tau_p} \leqslant kc_s(T_e), \tag{36}$$

which gives approximately

$$\frac{2\times 10^4}{\sqrt{T_e\,[\text{eV}]}} \leqslant \tau_p\,[\text{fs}] \quad \leftrightarrow \quad T_e\,[\text{eV}] \geqslant \frac{4\times 10^8}{\tau_p^2\,[\text{fs}^2]} \equiv T_e^{\text{crossover}}. \tag{37}$$

Here $T_e^{\text{crossover}}$ is the crossover temperature which depends on τ_p.

Note that in Fig. 11(a) for a very long pulse all temperature values satisfy $T_e > T_e^{\text{crossover}}$, while in Fig. 11(b) for a very short pulse we are in the opposite limit $T_e < T_e^{\text{crossover}}$. Therefore, we pose the question whether we can see the crossover when the crossover temperature $T_e^{\text{crossover}}$ lies in the middle of the investigated temperature range. The answer is yes. An example is shown in Fig. 13 for $\tau_p \approx 1000$ fs. The above formula leads to a crossover at $T_e^{\text{crossover}} = 400\,\text{eV}$.

The following trend appears to be general in nature: For $T_e < T_e^{\text{crossover}}$ a rather flat T_e dependence occurs [similar to that in Fig. 11(b)], while for $T_e > T_e^{\text{crossover}}$ an algebraic dependence [similar to that in Fig. 11(a)] is dominant.

It is now useful to identify a crossover in Fig. 12. Solving the relation (37) for τ_p, we can define a crossover via

$$\tau_p^{\text{crossover}}\,[\text{fs}] = \frac{2\times 10^4}{\sqrt{T_e\,[\text{eV}]}}. \tag{38}$$

Evaluating for the parameters of Fig. 12 we find $\tau_p^{\text{crossover}} \approx 2000$ fs for $T_e = 100\,\text{eV}$ and $\tau_p^{\text{crossover}} \approx 1400$ fs for $T_e = 200\,\text{eV}$, in agreement with the points at which the qualitative behavior changes.

It should be emphasized that the different scaling behavior on either side of the crossover values can be readily inferred from the behavior of $F\chi$ (see Fig. 10). If the finite-bandwidth domain lies within kc_s, any change in the boundaries induces relatively large changes in the weighted integral contributions. Conversely, if the boundaries lie far outside kc_s, the dominant contributions tend to cancel, and only minor changes occur upon shifting the limits.

IV. SUMMARY AND CONCLUSIONS

Various parameters govern the evolution of ponderomotively driven plasma gratings. In addition to the obvious pump pulse amplitude a_0, the literature has mainly discussed the parameters ν and μ. The parameter ν distinguishes between operation in the collective regime ($\nu \gg 1$) and in the trapping regime ($\nu < 1$). The parameter μ includes, among others, the electron temperature T_e, with $\mu > 1$ defining a high-temperature regime.

In this paper, we investigate an additional parameter, namely, the pump laser duration τ_p. Short pump duration generates short gratings, whereas larger τ_p produce long and fairly homogeneous gratings. A characteristic crossover occurs at $\tau_p \sim O(\tau_p^{\text{crossover}})$, where the latter depends on the typical ion response time.

Using Vlasov simulations, we were able to identify a fundamental difference between short and long gratings and to determine the following characteristic behavior. For long pulses, the Vlasov simulations predict the amplitude scaling $\delta n \sim a_0^2$. However, for shorter pulses a further reduction of amplitudes with decreasing τ_p occurs. The predicted T_e dependence of the amplitudes is particularly useful. For long pulses, we have $\delta n \sim T_e^{-1}$. However, depending on τ_p, a crossover point $T_e^{\text{crossover}}$ exists. Short pulses exhibit, at most, a very weak temperature dependence.

Using simple models, we clarified the fundamental behavior and also quantified it to a large extent. We employed a kinetic model based on Ref. [47], which was only slightly extended to account for a finite frequency spectrum. This model provides clear predictions for temperature and pulse-duration dependence. The kinetic finite-bandwidth model offers a solid understanding of the observations obtained from the Vlasov simulations. In practical applications, it is not always possible to employ very long pump pulses for grating generation. In such cases, the estimates obtained here indicate which strategy is most suitable and which configurations can be expected. In any case, ponderomotively driven gratings may last much longer than τ_p.

The modeling focuses on interpreting and contextualizing the results of complete Vlasov simulations. The aim is, above all, to develop physical intuition for grating formation. In this way, for specific cases, the most favorable situations for applications can be selected. After this narrowing down, the complete Vlasov simulation becomes the theoretical method of choice—but ultimately, as is customary in physics, experimental validation remains decisive.

DATA AVAILABILITY

There are no publicly available research data or software supporting this article. Requests for further information or data should be sent to the authors.

APPENDIX A: DURATION τ_p FOR A GAUSSIAN LASER PULSE

The electric field of a single laser pulse in vacuum propagating in the x direction with a Gaussian envelope is assumed as

$$E(x,t) = E_0 \exp\left(-\frac{(x - v_{g0}t)^2}{2\sigma_x^2}\right)\cos(k_0 x - \omega_0 t),$$

where E_0 is the peak electric field amplitude, v_{g0} is the group velocity of the pulse in vacuum which becomes $v_g = cN_0$, $N_0 = \sqrt{1 - \frac{n_0}{n_c}}$ in plasma, σ_x is the spatial width (standard deviation), k_0 is the central wavenumber, and ω_0 is the central angular frequency.

Following Ref. [32], we normalize t by $2\pi/\omega_0 \approx 2.67$ fs and x by $\lambda_0 = 800$ nm. Then we may write (normalized quantities with tilde)

$$\exp\left(\frac{-v_{g0}^2 t^2}{2\langle x^2\rangle}\right) \to \exp\left(\frac{-\tilde{t}^2 N_0^2}{2\langle \tilde{x}^2\rangle}\right) \equiv \exp\left(\frac{-\tilde{t}^2}{2\sigma_t^2}\right)$$
$$\text{with} \quad \sigma_t^2 = \frac{\langle \tilde{x}^2\rangle}{N_0^2}. \tag{A1}$$

We define the temporal width τ_p as its full width at half maximum (FWHM) via

$$\tau_p = 2\sqrt{2\ln 2}\,\sigma_t \approx 2.355\frac{\sqrt{\langle \tilde{x}^2\rangle}}{N_0}\,2.67\,\text{fs}. \tag{A2}$$

For $n_0/n_c = 0.05$ we obtain the relation

$$\tau_p\,[fs] \approx 6.45\sqrt{\langle \tilde{x}^2\rangle}. \tag{A3}$$

It is also possible to measure τ_p in ω_0^{-1} (introducing the parameter ll via $\tau_p = \frac{ll}{\omega_0} \approx \frac{ll}{2.35}$ [fs]).

For practical reasons, we sometimes approximate the laser pulse as a rectangular distribution. Then we get for the equivalent rectangular pulse with width τ_p an amplitude enhancement factor δ_a via

$$\int_{-\infty}^{+\infty} e^{-t^2/2\sigma_t^2}\,dt = \sqrt{2\pi}\sigma_t \equiv \tau_p\,\delta_a, \tag{A4}$$

i.e.,

$$\delta_a = \frac{\sqrt{2\pi}}{2.355} = 1.0644. \tag{A5}$$

APPENDIX B: PRESSURE VERSUS PONDEROMOTIVE FORCE

The (macroscopic) equation of motion for ions in the presence of pressure and ponderomotive force reads (in dimensional form)

$$\frac{\partial v_i}{\partial t} + v_i\frac{\partial v_i}{\partial x} = -\frac{1}{m_i}\left(\underbrace{\frac{\partial \varphi_p}{\partial x}}_{I} + \underbrace{\frac{1}{n_e}\frac{\partial P}{\partial x}}_{II}\right). \tag{B1}$$

There are two terms on the right-hand side which are often discussed separately.

Following Peng *et al.* [22] one may scale the ion velocity equation (B1) to a form that all coefficients are of order one.

Then we obtain Eq. 2(c) of Ref. [22],

$$\frac{\partial v_i}{\partial t} + v_i \frac{\partial v_i}{\partial x} = \underbrace{\sin x}_{I} - \underbrace{\mu \frac{\partial n_e^2}{\partial x}}_{II}, \tag{B2}$$

when the units

$$x_{\text{unit}} = \frac{1}{2k}, \quad t_{\text{unit}} = \sqrt{\frac{1}{2}\frac{m_e}{m_i}}(k v_0)^{-1}, \quad v_{\text{unit}} = \sqrt{\frac{1}{2}\frac{m_e}{m_i}} v_0 \tag{B3}$$

are used. From here we estimate the normalizing ion velocity in the hydrodynamic regime as

$$\bar{v}_i \approx 5 a_0 \frac{\text{nm}}{\text{fs}} = 5 \times 10^{-2} \frac{\text{nm}}{\text{fs}} \quad \text{for} \quad a_0 = 0.01 \text{ and protons.} \tag{B4}$$

The pressure contribution II dominates over the ponderomotive field contribution I when the $\mu \frac{\delta n}{n_0} > 1$, i.e., T_e [eV] $\gtrsim \frac{20}{\delta n / n_0}$.

[1] H. Hora, *Laser Plasma Physics: Forces and the Nonlinearity Principle*, 2nd ed. (SPIE Press, Bellingham, Washington, USA, 2016).

[2] C. H. Townes, *How the Laser Happened: Adventures of a Scientist* (Oxford University Press, 1999).

[3] D. Strickland and G. Mourou, Compression of amplified chirped optical pulses, Opt. Commun. **55**, 447 (1985).

[4] F. Krausz and M. Ivanov, Attosecond physics, Rev. Mod. Phys. **81**, 163 (2009).

[5] H. Milchberg, Indestructible plasma optics, Phys. Today **72**(6), 70 (2019).

[6] P. Michel, Plasma photonics: Manipulating light using plasmas, Tech. Rep. LLNL-TR-818220, Lawrence Livermore National Laboratory, 2021.

[7] C. Riconda and S. Weber, Plasma optics: A perspective for high-power coherent light generation and manipulation, Matter Radiat. Extremes **8**, 023001 (2023).

[8] V. Malkin, G. Shvets, and N. J. Fisch, Fast compression of laser beams to highly overcritical powers, Phys. Rev. Lett. **82**, 4448 (1999).

[9] Z.-M. Sheng, J. Zhang, and D. Umstadter, Plasma density gratings induced by intersecting laser pulses in underdense plasmas, Appl. Phys. B **77**, 673 (2003).

[10] A. A. Andreev, C. Riconda, V. T. Tikhonchuk, and S. Weber, Short light pulse amplification and compression by stimulated Brillouin scattering in plasmas in the strong coupling regime, Phys. Plasmas **13**, 053110 (2006).

[11] H.-C. Wu, Z.-M. Sheng, Q.-J. Zhang, Y. Cang, and J. Zhang, Manipulating ultrashort intense laser pulses by plasma Bragg gratings, Phys. Plasmas **12**, 113103 (2005).

[12] H.-C. Wu, Z.-M. Sheng, and J. Zhang, Chirped pulse compression in nonuniform plasma Bragg gratings, Appl. Phys. Lett. **87**, 201502 (2005).

[13] S. Suntsov, D. Abdollahpour, D. G. Papazoglou, and S. Tzortzakis, Femtosecond laser induced plasma diffraction gratings in air as photonic devices for high intensity laser applications, Appl. Phys. Lett. **94**, 251104 (2009).

[14] H. Y. Chen, Y. Yin, C. L. Tian, H. Xu, Y. Y. Ma, H. B. Zhuo, and F. Q. Shao, Moving electron density gratings induced in the beat-wave field of two counterpropagating laser pulses, Phys. Plasmas **17**, 083112 (2010).

[15] M. Durand, Y. Liu, B. Forestier, A. Houard, and A. Mysyrowicz, Experimental observation of a traveling plasma grating formed by two crossing filaments in gases, Appl. Phys. Lett. **98**, 121110 (2011).

[16] H. M. Milchberg, Y. H. Chen, Y. H. Cheng, N. Jhajj, J. P. Palastro, E. W. Rosenthal, S. Varma, J. K. Wahlstrand, and S. Zahedpour, The extreme nonlinear optics of gases and femtosecond optical filamentation, Phys. Plasmas **21**, 100901 (2014).

[17] M. R. Edwards, Z. Toroker, J. M. Mikhailova, and N. J. Fisch, The efficiency of Raman amplification in the wavebreaking regime, Phys. Plasmas **22**, 074501 (2015).

[18] G. Lehmann and K. H. Spatschek, Transient plasma photonic crystals for high-power lasers, Phys. Rev. Lett. **116**, 225002 (2016).

[19] G. Lehmann and K. H. Spatschek, Laser-driven plasma photonic crystals for high-power lasers, Phys. Plasmas **24**, 056701 (2017).

[20] G. Lehmann and K. H. Spatschek, Plasma-based polarizer and waveplate at large laser intensity, Phys. Rev. E **97**, 063201 (2018).

[21] G. Lehmann and K. H. Spatschek, Plasma photonic crystal growth in the trapping regime, Phys. Plasmas **26**, 013106 (2019).

[22] H. Peng, C. Riconda, M. Grech, J.-Q. Su, and S. Weber, Nonlinear dynamics of laser-generated ion-plasma gratings: A unified description, Phys. Rev. E **100**, 061201 (2019).

[23] H. Peng, C. Riconda, M. Grech, C.-T. Zhou, and S. Weber, Dynamical aspects of plasma gratings driven by a static ponderomotive potential, Plasma Phys. Control. Fusion **62**, 115015 (2020).

[24] C. Zhang, Z. Nie, Y. Wu, M. Sinclair, C.-K. Huang, K. A Marsh, and C. Joshi, Ionization induced plasma grating and its applications in strong-field ionization measurements, Plasma Phys. Control. Fusion **63**, 095011 (2021).

[25] H. H. Ma, S. M. Weng, P. Li, X. F. Li, Y. X. Wang, S. H. Yew, M. Chen, P. McKenna, and Z. M. Sheng, Growth, saturation, and collapse of laser-driven plasma density gratings, Phys. Plasmas **27**, 073105 (2020).

[26] H. Peng, C. Riconda, S. Weber, C. T. Zhou, and S. C. Ruan, Frequency conversion of lasers in a dynamic plasma grating, Phys. Rev. Appl. **15**, 054053 (2021).

[27] G. Lehmann and K. H. Spatschek, Reflection and transmission properties of a finite-length electron plasma grating, Matter Radiat. Extremes **7**, 054402 (2022).

[28] B.Y. Li, F. Liu, M. Chen, F. Y. Wu, J. W. Wang, L. Lu, J. L. Li, X. L. Ge, X. H. Yuan, W. C. Yan, L. M. Chen, Z. M. Sheng, and J. Zhang, Experimental demonstration of efficient harmonic generation via surface plasma compression with lasers, Phys. Rev. Lett. **128**, 244801 (2022).

[29] Z. Li, Y. Zuo, X. Zeng, Z. Wu, X. Wang, X. Wang, J. Mu, and B. Hu, Ultraintense few-cycle infrared laser generation by fast-extending plasma grating, Matter Radiat. Extremes **8**, 014401 (2023).

[30] Z. Wu, Y. Zuo, X. Zeng, Z. Li, Z. Zhang, X. Wang, B. Hu, X. Wang, J. Mu, J. Su, Q. Zhu, and Y. Dai, Laser compression via fast-extending plasma gratings, Matter Radiat. Extremes **7**, 064402 (2022).

[31] M. S. Hur, B. Ersfeld, H. Lee, H. Kim, K. Roh, Y. Lee, H. S. Song, M. Kumar, S. Yoffe, D. A. Jaroszynski, and H. Suk, Laser pulse compression by a density gradient plasma for exawatt to zettawatt lasers, Nat. Photonics **17**, 1074 (2023).

[32] G. Lehmann and K. H. Spatschek, Formation and properties of spatially inhomogeneous plasma density gratings, Phys. Rev. E **108**, 055204 (2023).

[33] M. Hu, S. Yuan, J. Nan, Y. Cao, J. Chen, and H. Zeng, Filamentation-induced volume plasma grating: Dynamics, possibilities, and advantages, Laser Photonics Rev. **17**, 2300310 (2023).

[34] I. E. Ochs and N. J. Fisch, Critical role of isopotential surfaces for magnetostatic ponderomotive forces, Phys. Rev. E **108**, 065210 (2023).

[35] K. V. Lezhnin, K. Qu, N. J. Fisch, and S. V. Bulanov, On parallel laser beam merger in plasmas, Phys. Plasmas **31**, 032114 (2024).

[36] G. Lehmann and K. H. Spatschek, Plasma-grating-based laser pulse compressor, Phys. Rev. E **110**, 015209 (2024).

[37] Z. J. Chen, Q. Wang, D. J. Liu, S. T. Zhang, R. J. Cheng, X. X. Li, S. Y. Lv, Z. M. Huang, Z. Y. Xu, Q. Wang, Z. J. Liu, L. H. Cao, and C. Y. Zheng, Pulse splitter using a moving space-time electron plasma grating, Phys. Rev. E **112**, 015203 (2025).

[38] Z. Wu, X. Zeng, Z. Li, X. Wang, J. Mu, H. Peng, K. Zhou, D. Hu, Y. Zuo, N. J. Fisch, C. Riconda, and S. Weber, Spatiotemporal plasma hologram, Optica **13**, 1020 (2026).

[39] N. Bonod and J. Neauport, Diffraction gratings: From principles to applications in high-intensity lasers, Adv. Opt. Photon. **8**, 156 (2016).

[40] J.-R. Marquès, L. Lancia, T. Gangolf, M. Blecher, S. Bolaños, J. Fuchs, O. Willi, F. Amiranoff, R. L. Berger, M. Chiaramello, S. Weber, and C. Riconda, Joule-level high-efficiency energy transfer to subpicosecond laser pulses by a plasma-based amplifier, Phys. Rev. X **9**, 021008 (2019).

[41] M. R. Edwards, V. R. Munirov, A. Singh, N. M. Fasano, E. Kur, N. Lemos, J. M. Mikhailova, J. S. Wurtele, and P. Michel, Holographic plasma lenses, Phys. Rev. Lett. **128**, 065003 (2022).

[42] M. R. Edwards and P. Michel, Plasma transmission gratings for compression of high-intensity laser pulses, Phys. Rev. Appl. **18**, 024026 (2022).

[43] M. R. Edwards, S. Waczynski, E. Rockafellow, L. Manzo, A. Zingale, P. Michel, and H. M. Milchberg, Control of intense light with avalanche-ionization plasma gratings, Optica **10**, 1587 (2023).

[44] M. R. Edwards, N. M. Fasano, A. M. Giakas, M. M. Wang, J. Griff-McMahon, A. Morozov, V. M. Perez-Ramirez, N. Lemos, P. Michel, and J. M. Mikhailova, Greater than five-order-of-magnitude postcompression temporal contrast improvement with an ionization plasma grating, Phys. Rev. Lett. **133**, 155101 (2024).

[45] H. Peng, J.-R. Marquès, L. Lancia, F. Amiranoff, R. L. Berger, S. Weber, and C. Riconda, Plasma optics in the context of high intensity lasers, Matter Radiat. Extremes **4**, 065401 (2019).

[46] H. Peng, C. Riconda, M. Grech, and S. Weber, Parametric description of laser-generated ion plasma gratings, in *Proceedings of 47th EPS Conference on Plasma Physics*, Europhysics Conference Abstracts Vol. 45A (European Physical Society, Mulhouse, France, 2021).

[47] P. Michel, W. Rozmus, E. A. Williams, L. Divol, R. L. Berger, S. H. Glenzer, and D. A. Callahan, Saturation of multi-laser beams laser-plasma instabilities from stochastic ion heating, Phys. Plasmas **20**, 056308 (2013).

[48] P. Michel, L. Divol, D. Turnbull, and J. D. Moody, Dynamic control of the polarization of intense laser beams via optical wave mixing in plasmas, Phys. Rev. Lett. **113**, 205001 (2014).

[49] P. Michel, E. Kur, M. Lazarow, T. Chapman, L. Divol, and J. S. Wurtele, Polarization-dependent theory of two-wave mixing in nonlinear media, and application to dynamical polarization control, Phys. Rev. X **10**, 021039 (2020).

[50] G. Lehmann, Efficient semi-Lagrangian Vlasov-Maxwell simulations of high order harmonic generation from relativistic laser-plasma interactions, Commun. Comput. Phys. **20**, 583 (2016).

[51] G. Lehmann and K. H. Spatschek, Temperature dependence of seed pulse amplitude and density grating in Brillouin amplification, Phys. Plasmas **23**, 023107 (2016).

[52] P. Mora and T. M. Antonsen, Jr., Kinetic modeling of intense, short laser pulses propagating in tenuous plasmas, Phys. Plasmas **4**, 217 (1997).